Meng *et al. Ageing Neur Dis* 2024;4:9
DOI: 10.20517/and.2023.15

Ageing and Neurodegenerative Diseases

Original Article

Open Access

Fibril-forming motif of non-expanded ataxin-3 revealed by scanning proline mutagenesis

Sheng-Rong Meng[1], Chao Ma[1], Jie Chen[1], Li-Qiang Wang[1], Hong-Yu Hu[2], Yi Liang[1,*]

[1]Hubei Key Laboratory of Cell Homeostasis, College of Life Sciences, TaiKang Center for Life and Medical Sciences, Wuhan University, Wuhan 430072, Hubei, China.
[2]State Key Laboratory of Molecular Biology, Shanghai Institute of Biochemistry and Cell Biology, Center for Excellence in Molecular Cell Science, Chinese Academy of Sciences, Shanghai 200031, China.

[*]**Correspondence to:** Prof. Yi Liang, Hubei Key Laboratory of Cell Homeostasis, College of Life Sciences, TaiKang Center for Life and Medical Sciences, Life Sciences Building, Wuhan University, No. 299, Bayi Road, Wuchang District, Wuhan 430072, China. E-mail: liangyi@whu.edu.cn

How to cite this article: Meng SR, Ma C, Chen J, Wang LQ, Hu HY, Liang Y. Fibril-forming motif of non-expanded ataxin-3 revealed by scanning proline mutagenesis. *Ageing Neur Dis* 2024;4:9. https://dx.doi.org/10.20517/and.2023.15

Received: 31 May 2023 **First Decision:** 11 Oct 2023 **Revised:** 9 May 2024 **Accepted:** 3 Jun 2024 **Published:** 11 Jun 2024

Academic Editor: Weidong Le **Copy Editor:** Dong-Li Li **Production Editor:** Dong-Li Li

Abstract

Aims: The misfolding of ataxin-3 in neurons is the hallmark of a neurodegenerative disease, spinocerebellar ataxia type 3 (SCA3), also known as Machado-Joseph disease (MJD). Ataxin-3 consists of a N-terminal Josephin domain and a C-terminal polyglutamine (polyQ) tract. The length of the polyQ tract is positively correlated with the disease. The aggregation of ataxin-3 *in vitro* is a two-step process, with the first step involving the aggregation of the Josephin domain and the second step involving an expanded polyQ tract. However, the fibril-forming motif of the Josephin domain is not well understood.

Methods: In this study, we employed 3D profile algorithm and scanning proline mutagenesis to identify the fibril-forming motif of non-expanded ataxin-3.

Results: By using thioflavin T fluorescence kinetics, sarkosyl-insoluble SDS-PAGE, transmission electron microscopy (TEM), and Fourier transform infrared spectroscopy (FTIR), we identified the fibril-forming motif of the Josephin domain of non-expanded ataxin-3 as ^{79}VISNAL^{84}.

Conclusions: We demonstrated that the proline mutation in the fibril-forming motif of the Josephin domain could inhibit the aggregation of expanded ataxin-3, which shows some therapeutic promise.

Keywords: Machado-Joseph disease, transmission electron microscopy, spinocerebellar ataxia type 3, ataxin-3, fibril-forming motif

INTRODUCTION

Protein misfolding is a pathological characteristic of neurodegenerative diseases, leading to the formation of amyloid fibrils. Polyglutamine (polyQ) diseases are a group of neurodegenerative diseases caused by the misfolding of proteins containing expanded polyQ tracts[1]. There are nine members in the polyQ disease family: spinal bulbar muscular atrophy, Huntington's disease, dentatorubral-pallidoluysian atrophy, and spinocerebellar ataxia (SCA) types 1, 2, 3, 6, 7, and 17[1-3].

Early research on polyQ diseases has focused on the relationship between the length of polyQ tract and diseases. Researchers have identified several shared features among polyQ diseases. First, the length of polyQ tract is in positive correlation with the risk of disease onset and in negative correlation with the age of disease onset. Second, intracellular aggregates and inclusions containing polyglutamine protein have been detected in tissues of all polyQ disease patients. Third, *in vitro* studies have shown that polyglutamine protein can form amyloid fibrils and the aggregation rate increases as the length of polyQ tract increases. Hereby, researchers have proposed the toxic gain of function hypothesis that polyQ diseases are caused by the aggregation of expanded polyQ tracts[4].

Although polyQ diseases share some features, each polyQ disease possesses distinctive symptomatology and pathology. PolyQ proteins are different in size, cellular localization, and biological function, implying that the toxic effect of a given polyQ expansion depends on the specific protein context[3].

SCA3 or Machado-Joseph disease (MJD) is the most common form of spinocerebellar ataxia. The gene associated with SCA3 is *ATXN3*, which is mapped to chromosome 14q32.1[5]. It encodes the protein ataxin-3 consisting of an N-terminal globular Josephin domain (JD) and a disordered C-terminus containing a polyQ tract and two or three ubiquitin interacting motifs (UIM)[6]. The non-pathogenic ataxin-3 in healthy individuals contains a polyQ tract with 13-41 glutamines and the pathogenic form in SCA3 patients contains a polyQ tract with 55-86 glutamines[7-9]. Previous articles have documented that SCA3 is caused by a $(CAG)_n$ expansion (60-87 tandem copies) in ataxin-3 and the normal expansion range is 12-44 repeats[10,11].

Some *in vitro* studies show that non-expanded ataxin-3 forms fibrils under certain conditions[1], including exposure to metal ions[12], high temperatures, and high pressures[13], as well as under physiological conditions[14-16]. The aggregation of non-expanded ataxin-3 is mainly contributed by the N-terminal globular Josephin domain. Researchers proposed a two-step process hypothesis for the misfolding of expanded ataxin-3. The first step is that the Josephin domain assembles into SDS soluble aggregates, and the second step is the SDS insoluble aggregates formed by an expanded polyQ tract[15].

Researchers have identified some important residues in the aggregation of the Josephin domain. Some bioinformatics methods including Aggrescan[17], Tango[18], Waltz[19], Pasta[20], and Zyggregator[21] indicated that residues 73-96 of the Josephin sequence have a high aggregation propensity[22]. Seeding experiments indicated that residues 73-96 can significantly reduce the aggregation lag time of non-expanded ataxin-3 and expanded ataxin-3[23]. Mutation I77K/Q78K and W87K can inhibit the aggregation of the Josephin domain[22]. Molecular dynamics simulations indicated that ^{84}LKVW^{87} exposes to solution after the structural global rearrangements caused by the interaction of Josephin domains[24].

The structure of the amyloid fibril contains cross- core and non-core domains. The sequence in the cross-core is called the fibril-forming motif that contains about 6 residues[25,26]. However, the fibril-forming motif of the Josephin domain is not well understood. In this study, we employed 3D profile algorithm and scanning proline mutagenesis to identify the fibril-forming motif of non-expanded ataxin-3. By using thioflavin T (ThT) fluorescence kinetics, transmission electron microscopy (TEM), Fourier transform infrared spectroscopy (FTIR), and other biophysical methods, we identified the fibril-forming motif of the Josephin domain as ^{79}VISNAL^{84}. We also demonstrated that the proline mutation in the fibril-forming motif of the Josephin domain inhibited the misfolding of expanded ataxin-3.

MATERIALS AND METHODS

Materials

ThT was purchased from Sigma-Aldrich (St. Louis, MO, USA). Dithiothreitol (DTT), sodium azide (NaN_3), and sarkosyl were obtained from Amresco (Solon, OH, USA).

Plasmid construction and protein purification

For prokaryotic expression, wild-type human Ataxin-3(22Q), Ataxin-3(45Q), and their mutations were constructed into the pET-22b(+) plasmids. Each kind of the protein included a C-terminal His tag (LEHHHHHH). All the His-tag fused proteins were overexpressed in E. coli BL21 (DE3) strain (Novagen) and purified by a Ni^{2+}-NTA column (GE Healthcare, NY, USA). Protein was stored at -80 °C.

3D profile algorithm prediction

To predict the fibril-forming motif of non-expanded ataxin-3, we used the 3D profile algorithm developed by Eisenberg's lab[27,28]. We searched the protein ataxin-3 in the database ZipperDB on line. The URL of the ZipperDB is http://services.mbi.ucla.edu/zipperdb/.

Fibril formation

50 μM ataxin-3 and its mutations were incubated at pH 7.4 in Tris-buffered saline (TBS) (10 mM Tris, 150 mM NaCl) containing 5 mM DTT and 0.05% NaN3. Reactions were performed at 37 °C without shaking.

ThT binding assays

A 2.5 mM ThT stock solution was freshly prepared in 10 mM TBS buffer (pH 7.0) and passed through a 0.22-μm pore size filter before use to remove insoluble particles. A series of 80 μL samples were taken in chronological order, and mixed with 320 μL of 10 mM TBS buffer and 3.2 μL of ThT stock solution before measurements. The fluorescence of ThT was excited at 440 nm with a slit width of 5.0 nm and the emission was measured at 480 nm with a slit width of 5.0 nm on an LS-55 luminescence spectrometer (PerkinElmer Life Sciences, Shelton, CT). Kinetic parameters were determined by fitting ThT fluorescence intensity *vs.* time to a Hill equation:

$$F(t) = F(\infty)\frac{(t/t_{50})^n}{1+(t/t_{50})^n}$$

Here $F(\infty)$ is the fluorescence intensity in the long time limit, t_{50} is the elapsed time at which F is equal to one-half of $F(\infty)$, and n is a cooperativity parameter.

Sarkosyl-insoluble SDS-PAGE

A series of 80 μL human Ataxin samples were taken in chronological order during fibril formation corresponding to ThT binding assays. 80 μL samples were added with 320 μL 1% sarkosyl. The mixture was left at room temperature for 2 h and then centrifugated on a CP100NX ultracentrifuge (Hitachi, Japan) at 150,000 *g* for 30 min. The supernatant (sarkosyl-soluble ataxin-3) was removed, and the pellet (sarkosyl-insoluble ataxin-3) was resuspended in 30 mL of 2× SDS loading buffer containing 5% β-mercaptoethanol and subjected to 15% SDS-PAGE. After the electrophoresis, the gels were stained by Coomassie blue R250.

TEM

Sample aliquots of 10 μL were placed on copper grids and left at room temperature for 1-2 min, rinsed twice with H_2O, and then stained with 2% (w/v) uranyl acetate for another 1-2 min. The stained samples were examined using an H-8100 (or an H-7000 FA) transmission electron microscope (Hitachi, Tokyo, Japan) operating at 100 kV.

Circular dichroism spectroscopy

Circular dichroism (CD) spectra were obtained by using a Jasco J-810 spectropolarimeter (Jasco Corp., Tokyo, Japan) with a thermostated cell holder. Quartz cell with a 1 mm light path was used for measurements in the far-ultraviolet (far-UV) region. Spectra were recorded from 195 to 250 nm for far-UV CD.

FTIR

Attenuated total reflection FTIR spectra were recorded using a Nicolet 5700 FTIR spectrophotometer (Thermo Electron, Madison, WI).

Cell culture and transfection

SH-SY5Y neuroblastoma cells were cultured in Dulbecco's modified Eagle's medium (DMEM) supplemented with 10% (v/v) fetal bovine serum (FBS), 100 U/mL penicillin, and 100 U/mL streptomycin in 5% CO_2 at 37 °C. SH-SY5Y cells were transiently transfected with FLAG-tagged human ataxin-3 in phage vector using Lipofectamine® 2000 (Invitrogen, Carlsbad, CA) according to the manufacturer's protocol.

Confocal microscopy

SH-SY5Y cells transiently over-expressing FLAG-tagged wild-type ataxin-3 and mutants were cultured in media for 48 h. Cells were fixed with 4% paraformaldehyde, ruptured with 0.25% Triton-X 100, stained with 0.1% thioflavin S (ThS), coimmunostained with primary monoclonal antibodies anti-FLAG and secondary Alexa Fluo-546, and visualized by confocal microscopy.

RESULTS

Fibril-forming motif predicted by 3D profile algorithm

To predict the fibril-forming motif of non-expanded ataxin-3, we used the 3D profile algorithm developed by Eisenberg's lab[27,28]. This algorithm has been successfully used to predict the fibril-forming motif of Tau[27] and SOD1[29]. 3D profile algorithm is a structure-based algorithm. This algorithm uses the crystal structure of the fibril-forming peptide NNQQNY from the sup35 prion protein which makes up the cross-spine of amyloid-like fibrils[30]. Each six-residue peptide not containing a proline from a putative protein sequence is threaded onto the NNQQNY structure backbone, and the energetic fit is evaluated by using the RosettaDesign program[31]. To avoid problems with their disulfide bonding abilities, cysteines were substituted for serines during modeling. Segments with energies below the threshold of -23 kcal/mol are deemed to have high fibrillation propensity[28].

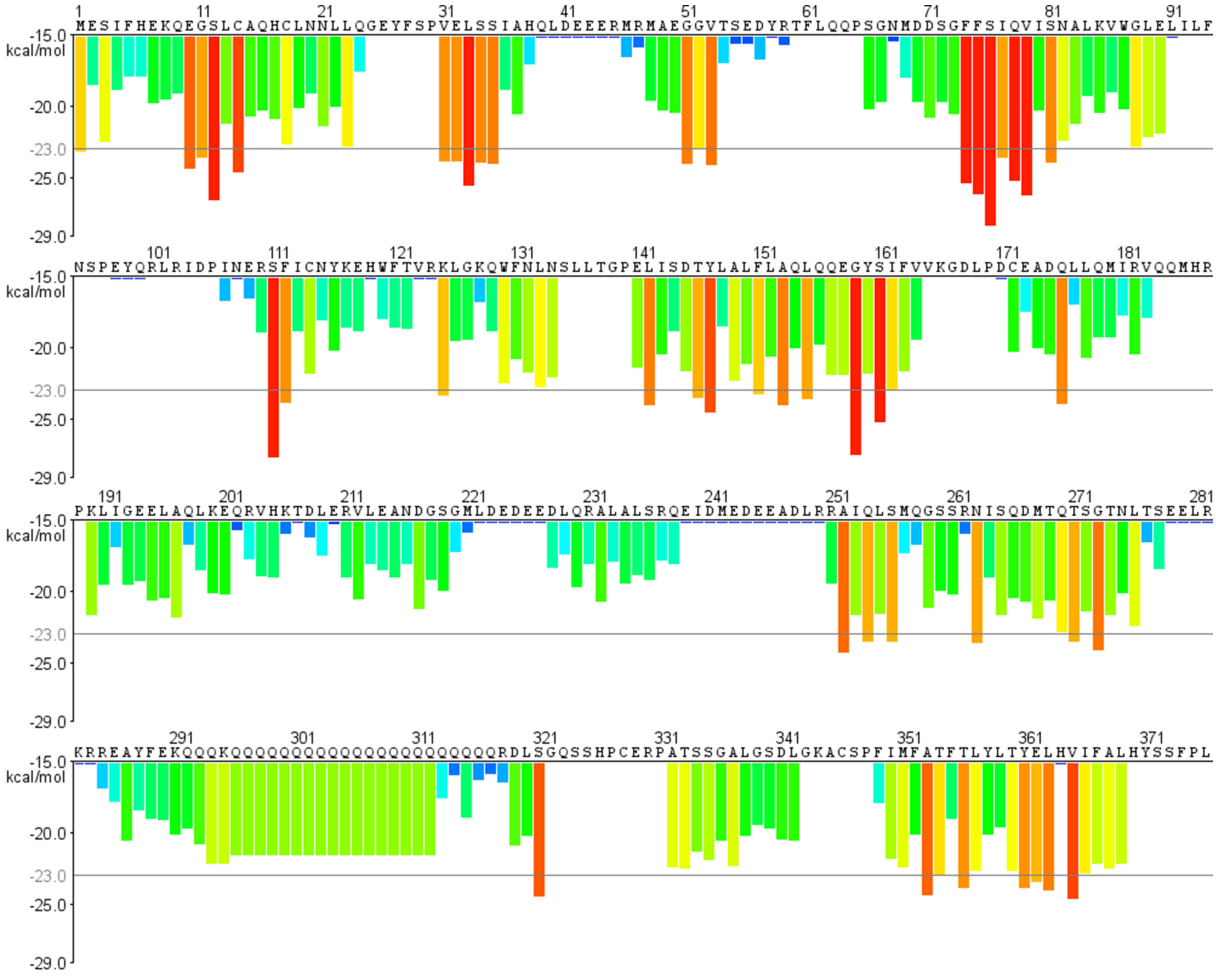

Figure 1. Most of the hexapeptides of non-expanded ataxin-3 did not tend to form fibrils. Diagram of the 3D-profile Rosetta energies (y-axis) calculated for each six-residue segment from the ataxin-3 sequence (x-axis). Segments predicted to form fibrils are highlighted in red.

The Rosetta energies of sequential hexapeptides of non-expanded ataxin-3 are plotted in Figure 1. The green columns mean that the Rosetta energies are above the threshold of -23 kcal/mol (gray line), and the red columns mean that the Rosetta energies are below the threshold of -23 kcal/mol. We found that most of the columns are green, indicating that most of the hexapeptides do not tend to form fibrils [Figure 1]. Some of the hexapeptides are not included in the profile because they contain prolines which are β-strand breakers.

We arranged the hexapeptides from low to high according to the Rosetta energies. The results of the top ten hexapeptides are shown in Table 1. We found that five of the top ten hexapeptides are located at 74-84. They are ^{76}SIQVIS^{81}, ^{79}VISNAL^{84}, ^{75}FSIQVI^{80}, ^{74}FFSIQV^{79}, and ^{78}QVISNA^{83}. Ricchelli *et al.* have predicted that 73-96 is the aggregation-prone region of ataxin-3 by other computer algorithms, supporting our conclusion[12].

Fibril-forming motif identified by scanning proline mutagenesis

The secondary structure of the core of amyloid is the β-sheet. As the β-sheet breaker, proline inhibits the fibrillization of proteins[32]. Scanning proline mutagenesis has been successfully used in identifying the fibril-forming motif of α-crystallin[33], Sup35 prion protein[34], and $A\beta_{40}$[35]. Thus, we investigated every scanning proline mutation from F74P to L89P in this manuscript.

Table 1. The top ten hexapeptides with the lowest Rosetta energy

Position	Sequence	Rosetta energy (kcal/mol)
76-81	SIQVIS	-28.300
111-116	SFICNY	-27.600
159-164	GYSIFV	-27.400
12-17	SLCAQH	-26.500
79-84	VISNAL	-26.200
75-80	FSIQVI	-26.100
33-38	LSSIAH	-25.500
74-79	FFSIQV	-25.300
161-166	SIFVVK	-25.200
78-83	QVISNA	-25.200

Based on the bioinformatics method of 3D-profile, we constructed proline mutation from F74, using the ataxin-3(22Q) as a template. We expressed and purified the proline mutations from *Escherichia coli* and incubated them under physiological conditions. We initially analyzed ThT fluorescence kinetics for the aggregation of all ataxin-3 mutations. The results of ThT fluorescence kinetics are shown in Figure 2 and the fitting data in Table 2. The wild-type ataxin-3(22Q) forms ThT-positive aggregates under physiological conditions, and the kinetic curve of the wild-type follows an S pattern, consistent with a nucleation-polymerization model [Figure 2]. Different mutations have different influences on ataxin-3(22Q) and the main affected parameter is $F(\infty)$ [Figure 2]. Figure 2 presents the intuitive comparison of the $F(\infty)$ of different mutations. The $F(\infty)$ of wild-type ataxin-3(22Q) is the highest, and from ataxin-3(22Q)/F74P, the $F(\infty)$ gradually decreased. The $F(\infty)$ of Ataxin-3(22Q)/I80P and Ataxin-3(22Q)/A83P is the lowest. The $F(\infty)$ of Ataxin-3(22Q)/V86P and Ataxin-3(22Q)/L89P is higher than Ataxin-3(22Q)/I80P and Ataxin-3(22Q)/A83P, but significantly lower than wild-type ataxin-3(22Q) [Table 2]. The $F(\infty)$ of Ataxin-3(22Q)/I92P is close to wild-type ataxin-3(22Q). Another parameter t_{50} showed no regularity in the changes [Table 1].

We then analyzed the aggregation kinetics by sarkosyl-insoluble SDS-PAGE [Figure 3]. Sarkosyl is commonly used to purify proteins from inclusion bodies[36]. As a mild detergent, sarkosyl has also been used to extract the fibrils of Tau protein from the brain tissue of Alzheimer's disease[37] and the fibrils of α-synuclein from the brain tissue of Parkinson's disease[38]. Moreover, this detergent has been used in quantitative analysis of amyloid fibrils[39-42]. In order to locate the fibril-forming motif more precisely, we investigated every scanning proline mutation from F74P to L89P. The wild-type ataxin-3(22Q) formed sarkosyl-insoluble fibrils after 1 day and then the sarkosyl-insoluble fibrils increased until 3 days [Figure 3]. The sarkosyl-insoluble SDS-PAGE change of ataxin-3(22Q)/F74P was similar to the wild-type ataxin-3(22Q) [Figure 3]. From the mutations F75P to Q78P, the sarkosyl-insoluble fibrils formed later and later. From the mutations of V79P to L84P, the proteins did not form sarkosyl-insoluble fibrils even upon the incubation time of up to 7 days. From the mutation of K85P to L89P, the proteins restored the capacity to form sarkosyl-insoluble fibrils gradually [Figure 3]. However, until the mutation L89P, the aggregation of proline mutation was still slower than wild-type ataxin-3(22Q) [Figure 3]. Combining ThT fluorescence kinetics and sarkosyl-insoluble SDS-PAGE results, we located the fibril-forming motif of non-expanded ataxin-3 at ^{79}VISNAL^{84}.

Next, we observed the fibril morphology of different proline mutations by TEM [Figure 4]. The amyloid fibrils of wild-type ataxin-3(22Q) were worm-like with a diameter of 10-20 nm and a length of 100-200 nm,

Table 2. Kinetic parameters for the aggregation of ataxin-3(22Q), ataxin-3(45Q), and their mutations

	$F(\infty)$	t_{50} (h)	n
22Q	656.9 ± 9.9	26.7 ± 0.9	3.5 ± 0.5
22Q/F74P	523.6 ± 8.3	24.6 ± 0.9	2.9 ± 0.4
22Q/I77P	425.8 ± 59.7	93.3 ± 21.4	1.3 ± 0.2
22Q/I80P	114.3 ± 15.1	16.9 ± 4.2	1.2 ± 0.8
22Q/A83P	139.1 ± 22.2	23.5 ± 6.0	1.3 ± 0.8
22Q/V86P	206.8 ± 8.8	19.1 ± 2.8	2.3 ± 1.0
22Q/L89P	210.0 ± 7.5	10.5 ± 2.0	1.2 ± 0.4
22Q/I92P	484.3 ± 25.2	60.8 ± 3.6	4.4 ± 1.0
22Q/I80A	440.2 ± 8.7	17.4 ± 8.0	4.5 ± 6.5
22Q/6G	245.3 ± 18.0	20.3 ± 4.0	2.1 ± 1.3
45Q	808.4 ± 4.5	7.1 ± 0.7	2.4 ± 0.4
45Q/I80P	189.1 ± 14.0	6.8 ± 3.6	1.4 ± 1.1

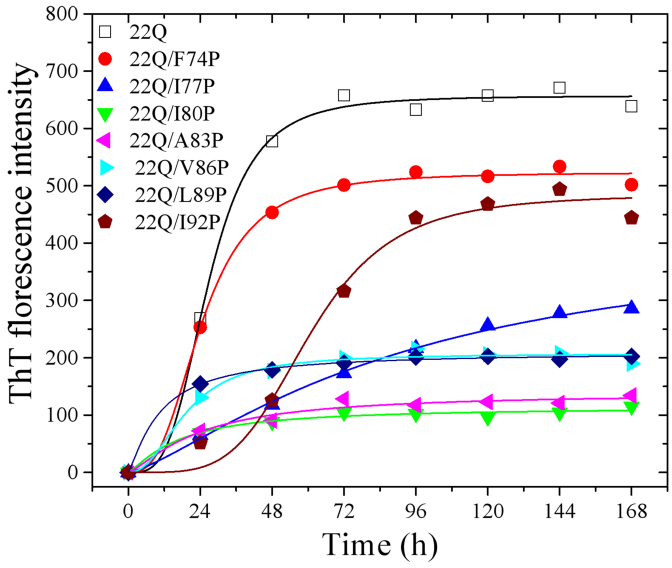

Figure 2. Different mutations have different influences on ataxin-3(22Q). Kinetic curves for the aggregation of ataxin-3(22Q) (black), F74P (red), F75P (green), S76P (blue), I77P (magenta), I80P (wine), A83P (navy), and V86P (pink), monitored by ThT fluorescence. The concentration of ataxin-3(22Q) and mutations was 50 M, and 10 mM TBS buffer (pH 7.4) containing 5 mM DTT was used. The assays were carried out at 37 °C, and the observation time was 168 h. DTT: Dithiothreitol.

and the fibrils of ataxin-3(22Q)/F74P were not significantly different from the wild-type ataxin-3(22Q) [Figures 4A and B]. Ataxin-3(22Q)/S81P and ataxin-3(22Q)/N82P did not form worm-like fibrils but produced amorphous aggregates, and the ataxin-3(22Q)/L89P formed short worm-like fibrils [Figures 4C-E]. The fibrils of ataxin-3(22Q)/I92P were not significantly different from the wild-type ataxin-3(22Q) [Figure 4F].

The changes in secondary structures of the wild-type ataxin-3(22Q) and its proline mutations were monitored using far-UV CD spectroscopy [Figure 5] and FTIR [Figure 6]. On day 0, the wild-type ataxin-3(22Q) and its proline mutations showed similar CD spectra, having double minima at 208 and 222 nm [Figures 5A-F], indicative of predominant α-helical structure. On day 3, the CD spectra of the wild-type ataxin-3(22Q) changed with a new minimum around 216 nm [Figure 5A], indicating the formation of

Figure 3. Different mutations have different influences on ataxin-3(22Q) based on time-dependent SDS-PAGE analysis. 50 μM ataxin-3(22Q) or proline mutations were incubated in 10 mM TBS buffer (pH 7.4) at 37 °C. Aliquots were taken at 0, 1, 2, 3, 4, 5, 6, and 7 days, respectively, and then incubated with TBS buffer containing 1% sarkosyl followed by centrifuging at 150,000 × *g* for 30 min. Pellets were resuspended with sample buffer containing 5% 2-mercaptoethanol and subjected to 15% SDS-PAGE. Gels were stained with Coomassie Blue. TBS: Tris-buffered saline.

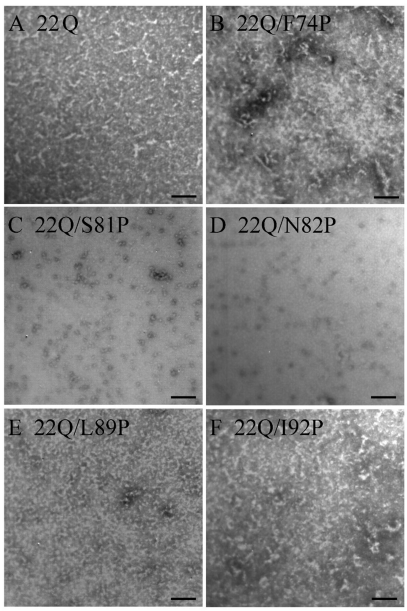

Figure 4. Different mutations have different influences on ataxin-3(22Q) fibril morphology based on TEM measurements of the Ataxin-3(22Q) and proline mutations. Negative-stain transmission electron micrographs of the following mutants: (A) ataxin-3(22Q); (B) ataxin-3(22Q)/F74P; (C) ataxin-3(22Q)/S81P; (D) ataxin-3(22Q)/N82P; (E) ataxin-3(22Q)/L89P; (F) and ataxin-3(22Q)/I92P. The concentration of ataxin-3(22Q) and mutations was 50 M, and 10 mM TBS buffer (pH 7.4) containing 5 mM DTT was used. The assays were carried out at 37 °C, and the observation time was 3 days. The scale bars represent 200 nm. TEM: Transmission electron microscopy; DTT: dithiothreitol.

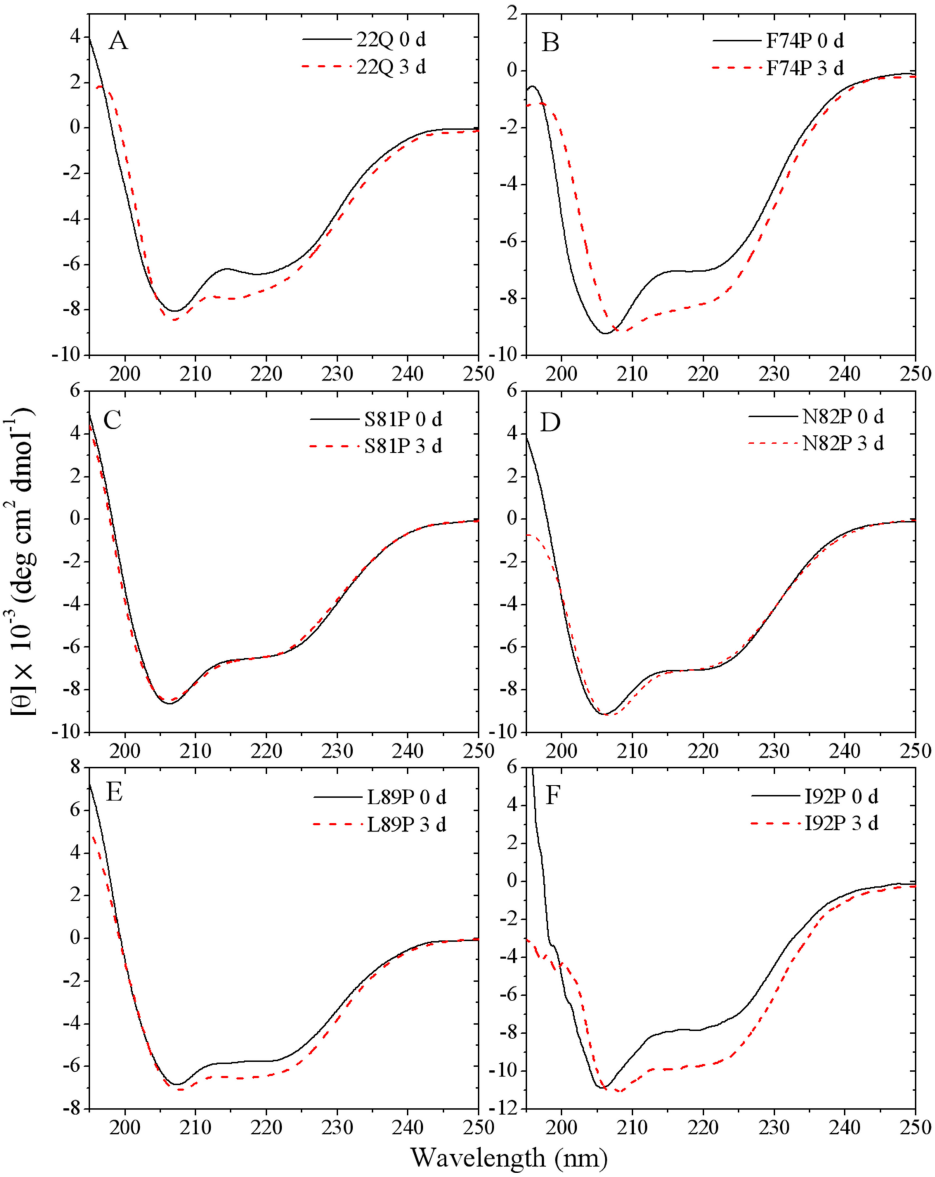

Figure 5. The fibril-forming motif of the Josephin domain was identified based on CD measurements of ataxin-3(22Q) and proline mutations. Far-UV CD spectra of the following mutations: (A) ataxin-3(22Q); (B) ataxin-3(22Q)/F74P; (C) ataxin-3(22Q)/S81P; (D) ataxin-3(22Q)/N82P; (E) ataxin-3(22Q)/L89P; and (F) ataxin-3(22Q)/I92P. The experimental conditions are the same as those in Figure 4. CD: Circular dichroism; far-UV: far-ultraviolet.

amyloid fibrils with predominant β-sheet structure. The CD spectra change of ataxin-3(22Q)/F74P and ataxin-3(22Q)/I92P was similar to the wild-type ataxin-3(22Q) [Figures 5B and F]. In contrast, the proline mutation in fibril-forming motif prevented the CD spectra changes after 3 days, which means that proline mutation in fibril-forming motif cannot form β-structure [Figures 5C and D]. The ataxin-3(22Q)/L89P underwent a slight structural change [Figure 5F]. Compared with CD spectroscopy, FTIR is more sensitive to β-structure. On day 0, the wild-type ataxin-3(22Q) and its proline mutations showed similar FTIR spectra, having an absorption peak at 1,655 cm^{-1} [Figure 6A], indicative of predominant α-helical structure. After 3 days, the absorption peak of the wild-type ataxin-3(22Q) was still at 1,655 cm^{-1} but with a significant rise at 1,625 cm^{-1} [Figure 6A], indicating the formation of amyloid fibrils with predominant β-sheet

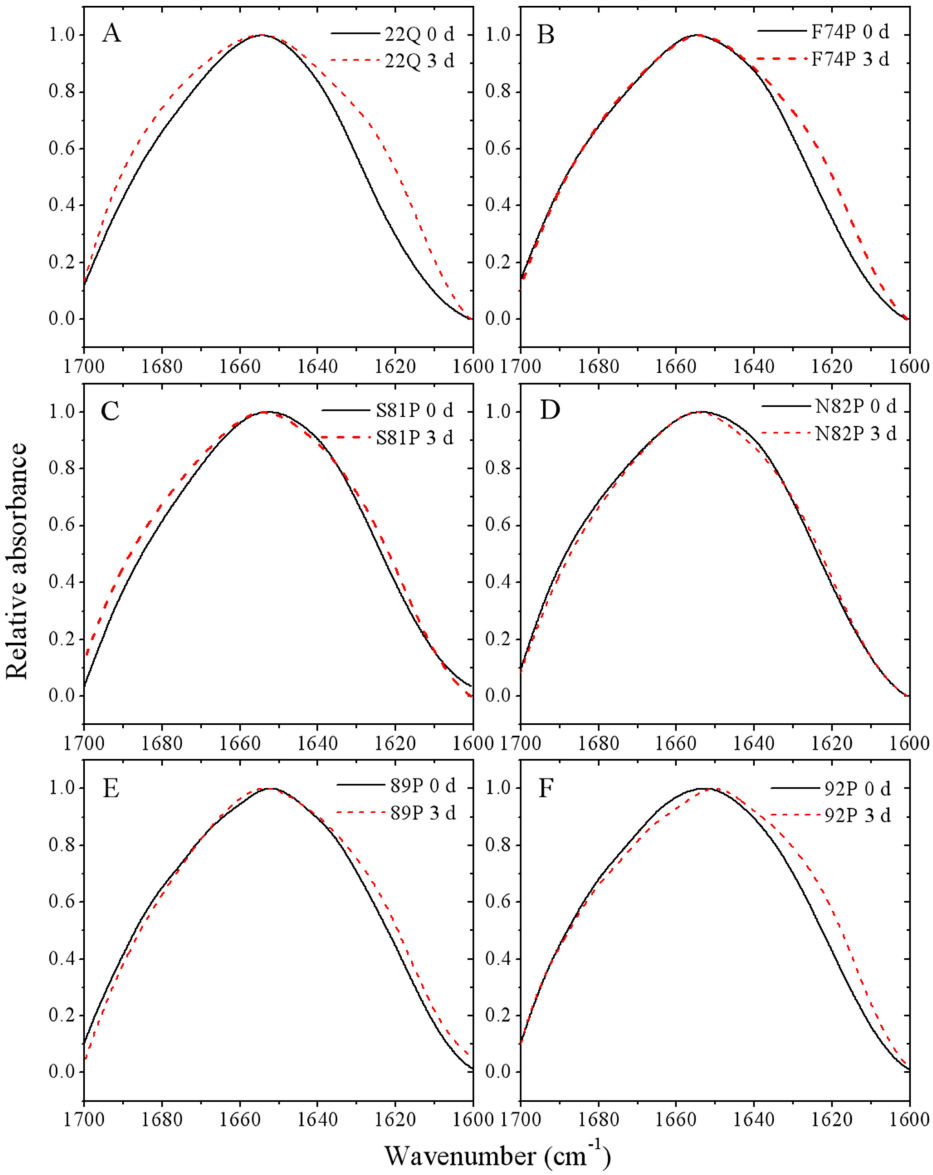

Figure 6. The fibril-forming motif of the Josephin domain was identified based on FTIR measurements of ataxin-3(22Q) and proline mutations. FTIR of the following mutations: (A) ataxin-3(22Q); (B) ataxin-3(22Q)/F74P; (C) ataxin-3(22Q)/S81P; (D) ataxin-3(22Q)/N82P; (E) ataxin-3(22Q)/L89P; and (F) ataxin-3(22Q)/I92P. The experimental conditions are the same as those in Figure 4. FTIR: Fourier transform infrared spectroscopy.

structure. The FTIR spectra change of ataxin-3(22Q)/F74P was similar to that of wild-type ataxin-3(22Q) and underwent a remarkable rise at 1,625 cm^{-1} [Figure 6B], and the FTIR spectra change of ataxin-3(22Q)/I92P was similar to ataxin-3(22Q)/F74P [Figure 6F]. In contrast, the proline mutation in fibril-forming motif prevented the FTIR spectra changes after 3 days [Figures 6C and D].

Collectively, by using ThT fluorescence kinetics, sarkosyl-insoluble SDS-PAGE, TEM, circular dichroism, and FTIR, we identified the fibril-forming motif of the Josephin domain as ^{79}VISNAL^{84}.

Alanine mutation in fibril-forming motif did not affect the aggregation of non-expanded ataxin-3

Alanine mutation has been frequently used in neutral mutation to study the function of amino acids because the side chain of alanine is methyl. We used alanine mutation as a control to demonstrate that the aggregation of non-expanded ataxin-3 is caused by the fibril-forming motif sequence but not hydrophobic residues. We mutated the 80th amino acid isoleucine to alanine. The Rosetta energy of the new sequence VASNAL is -25.600 kcal/mol, which is higher than VISNAL [Table 2] but lower than the threshold of -23 kcal/mol, so we speculated that ataxin-3(22Q)/I80A would not significantly affect the aggregation of ataxin-3(22Q).

The kinetic parameter $F(\infty)$ of ataxin-3(22Q)/I80A was remarkably lower than that of wild-type ataxin-3(22Q), consistent with the Rosetta energy [Figure 7A and Table 2]. The fibril morphology of ataxin-3(22Q)/I80A was worm-like, consistent with that of wild-type ataxin-3(22Q) [Figure 7B]. The sarkosyl-insoluble fibrils formed after 2 days, which is later than the wild-type ataxin-3(22Q) [Figure 7C]. The CD spectra of ataxin-3(22Q)/I80P were similar to the wild-type ataxin-3(22Q). After incubated under physiological conditions for 3 days, the ellipticity between 215 to 220 nm reduced [Figure 7D], indicating the formation of amyloid fibrils with predominant β-sheet structure, similar to wile-type ataxin-3(22Q). From the FTIR results, we reached the same conclusion [Figure 7E]. Collectively, alanine mutation in fibril-forming motif did not affect the misfolding of non-expanded ataxin-3.

All residues in fibril-forming motif mutated to glycine inhibit the misfolding of non-expanded ataxin-3

According to the steric zipper model, cross-β structure is constituted by the complementary side chains of two β-sheets[43]. Because glycine is the smallest amino acid whose side chain is a hydrogen atom, glycine residue is not beneficial to the formation of cross-β structure.

Therefore, polyglycine mutation is usually used as a negative control for research of fibril-forming motifs[43]. We mutated VISNAL to GGGGGG and named the mutation ataxin-3(22Q)/6G. The Rosetta energy of GGGGGG calculated by 3D profile algorithm is -18.200 kcal/mol, which is significantly higher than the threshold of -23 kcal/mol. Therefore, we speculated that ataxin-3(22Q)/6G would not form fibrils or remarkably inhibit aggregation.

The kinetic parameter $F(\infty)$ of ataxin-3(22Q)/6G was significantly lower than the wild-type ataxin-3(22Q), consistent with the Rosetta energy [Figure 7A and Table 2]. The worm-like fibril morphology could be observed by TEM for ataxin-3(22Q)/6G, but the fibril length was shorter and the fibrils were fewer than the wild-type ataxin-3(22Q) [Figure 7B]. The sarkosyl-insoluble fibrils formed after 3 days, which is later than the wild-type ataxin-3(22Q) [Figure 7C]. After being incubated under physiological conditions for 3 days, the ellipticity between 215 and 220 nm decreased [Figure 7D], indicating the formation of amyloid fibrils with predominant β-sheet structure, similar to wile-type ataxin-3(22Q). From the FTIR results, we reached the same conclusion [Figure 7E]. Taken together, all residues in fibril-forming motif mutated to glycine inhibited the misfolding of non-expanded ataxin-3.

Proline mutation in fibril-forming motif also inhibits the misfolding of expanded ataxin-3

All our research objects above were non-expanded ataxin-3. We also want to know the character of the fibril-forming motif in the aggregation of expanded ataxin-3. Bottomley's lab has found that small heat shock protein αB-crystallin interacts with the Josephin domain to inhibit the aggregation of the Josephin domain and the aggregation of ataxin-3(64Q)[44]. Therefore, we speculated that proline mutation in fibril-forming motifs would also inhibit the misfolding of expanded ataxin-3. We constructed mutation ataxin-3(45Q)/I80P and compared its aggregation ability with ataxin-3(45Q).

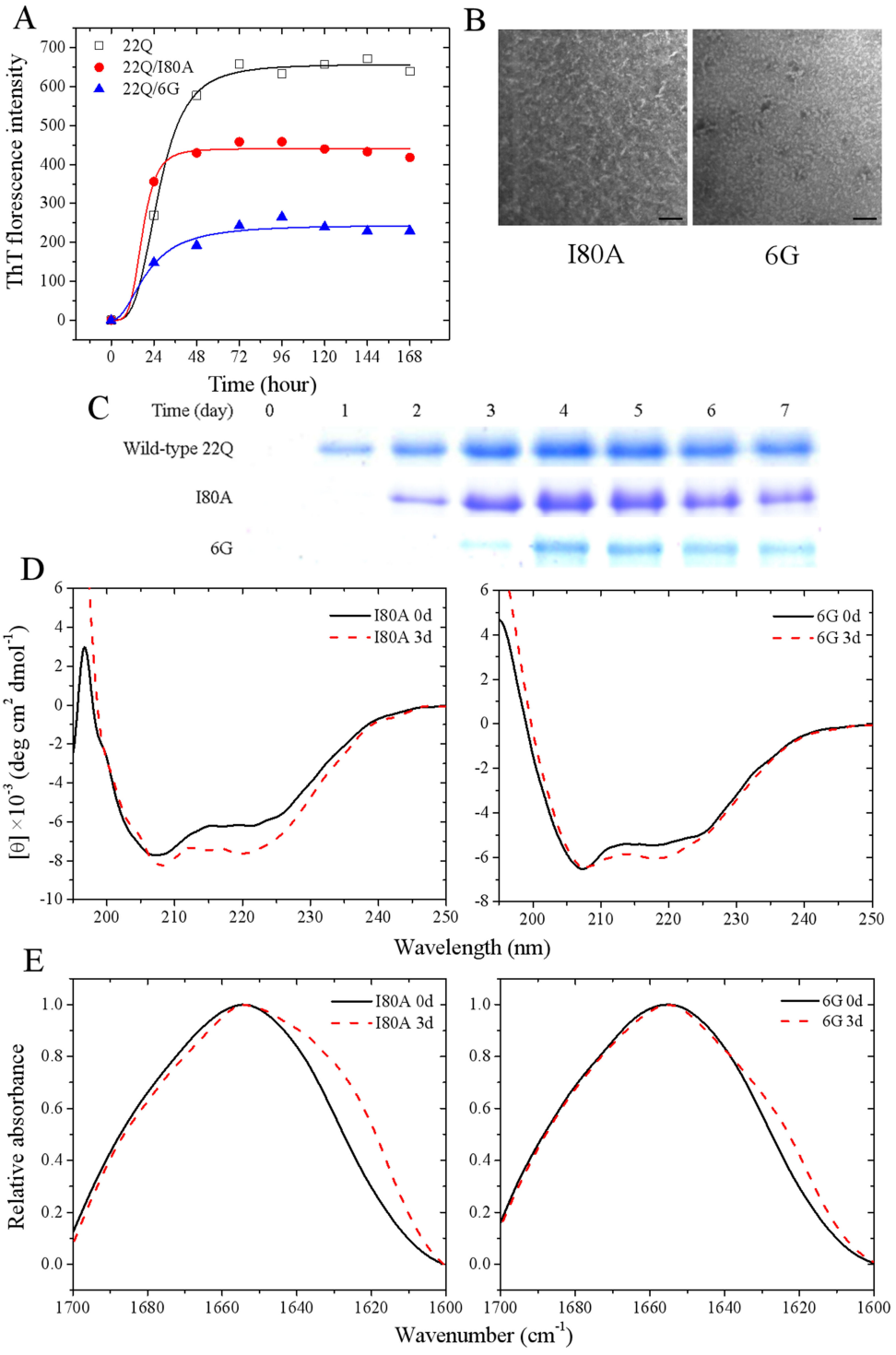

Figure 7. All residues in fibril-forming motif mutated to glycine inhibit the aggregation of non-expanded ataxin-3. (A) ThT binding assays of ataxin-3(22Q), ataxin-3(22Q)/I80A, and ataxin-3(22Q)/6G. The kinetic curves are fitted with Hill function; (B) TEM measurements of ataxin-3(22Q)/I80A (left) and ataxin-3(22Q)/6G (right); (C) Time-dependent SDS-PAGE analysis of sarkosyl-insoluble ataxin-3(22Q), ataxin-3(22Q)/I80A, and ataxin-3(22Q)/6G. The scale bars represent 200 nm; (D) CD measurements of ataxin-3(22Q)/I80A (left) and ataxin-3(22Q)/6G (right); (E) FTIR measurements of ataxin-3(22Q)/I80A (left) and ataxin-3(22Q)/6G (right). ThT: thioflavin T; TEM: transmission electron microscopy; CD: circular dichroism; FTIR: Fourier transform infrared spectroscopy.

Compared with ataxin-3(22Q), the kinetic parameter $F(\infty)$ of ataxin-3(45Q) was higher and t_{50} was lower [Table 2], indicating that the fibrillization rate of ataxin-3(45Q) is faster than ataxin-3(22Q). The kinetic parameter $F(\infty)$ of ataxin-3(45Q)/I80P was significantly lower than ataxin-3(45Q) [Figure 8A and Table 2]. After 2 days, ataxin-3(45Q)/I80P produced very small amounts of sarkosyl-insoluble fibrils [Figure 8B]. The fibril morphology of ataxin-3(45Q) was significantly different from ataxin-3(22Q), and the fibril length of ataxin-3(45Q) was more than 200 nm, which was longer than ataxin-3(22Q) [Figure 8B], suggesting that the expanded polyQ participated in fibril-forming of expanded ataxin-3 and changed the fibril morphology. Ataxin-3(45Q)/I80P also formed fibril observed by TEM, and the fibril morphology of ataxin-3(45Q)/I80P was similar to but shorter than ataxin-3(45Q) [Figure 8B]. The sarkosyl-insoluble fibrils formed after 2 days, which is later than ataxin-3(45Q) [Figure 8C]. The CD spectra of ataxin-3(45Q)/I80P was similar to ataxin-3(45Q). After being incubated under physiological conditions for 3 days, the ellipticity between 215 nm to 220 nm reduced [Figure 8D], indicating the formation of amyloid fibrils with predominant β-sheet structure, similar to ataxin-3(45Q). From the FTIR results, we reached the same conclusion [Figure 8E]. Collectively, mutation I80P inhibited the aggregation of ataxin-3(45Q).

Sequence-dependent abnormal aggregation of non-expanded ataxin-3 and expanded ataxin-3 in SH-SY5Y cells

We wanted to know the character of the fibril-forming motif in the aggregation of non-expanded ataxin-3. We found that wild-type ataxin-3(22Q) [Figure 9A] and ataxin-3(22Q)-F74P [Figure 9B] over-expressed in SH-SY5Y neuroblastoma cells did form aggregates in the cells. In sharp contrast, no aggregates were observed in either ataxin-3(22Q)-I80P [Figure 9C] or ataxin-3(22Q)-A83P [Figure 9D]. The above results demonstrated the sequence-dependent abnormal aggregation of ataxin-3(22Q) in SH-SY5Y cells and identified the fibril-forming motif of the Josephin domain in cells as ^{79}VISNAL^{84}.

We also wanted to know the character of the fibril-forming motif in the aggregation of expanded ataxin-3. We found that wild-type ataxin-3(45Q) [Figure 10A], ataxin-3(45Q)-F74P mutant [Figure 10B], and ataxin-3(45Q)-I92P mutant [Figure 10C] overexpressed in SH-SY5Y cells did form aggregates in the cells. In sharp contrast, no aggregates were observed in ataxin-3(45Q)-I80P [Figure 10D]. The above results demonstrated the sequence-dependent abnormal aggregation of ataxin-3(45Q) in SH-SY5Y cells.

It should be mentioned that in this manuscript, we defined ataxin-3(45Q) as an expanded ataxin-3. But this can only be considered an intermediate amplification range. The pathogenic expansion (full penetrance) of ataxin-3 requires more than 60 repeats. We plan to perform the experiments larger than ataxin-3(60Q) in the near future.

DISCUSSION

The misfolding of ataxin-3 in neurons is the hallmark of SCA3. Ataxin-3 is a polyQ protein, and the length of polyQ tract positively correlates with the risk of disease onset[6]. Expanded polyQ tract can aggregate itself or drive the context proteins to aggregate[15]. It has been found that the N-terminal Josephin domain plays a key role in the aggregation of non-expanded and expanded ataxin-3[14-16]. The Josephin domain aggregates before the expanded poly tract, suggesting that there are some other fibril-forming motifs besides polyQ tract. We further discuss the role of the fibril-forming motif of the Josephin domain in non-expanded and expanded ataxin-3. The fibril-forming motif of the Josephin domain determines the stability and aggregation properties of non-expanded ataxin-3[45], but the expansion of a polyglutamine tract in ataxin-3 leads to SCA3[46]. In this study, we explored the impact of specific amino acids on the misfolding properties of ataxin-3, the protein involved in SCA3 when polyglutamine expanded. We employed 3D profile algorithm and scanning proline mutagenesis to identify the fibril-forming motif of non-expanded ataxin-3

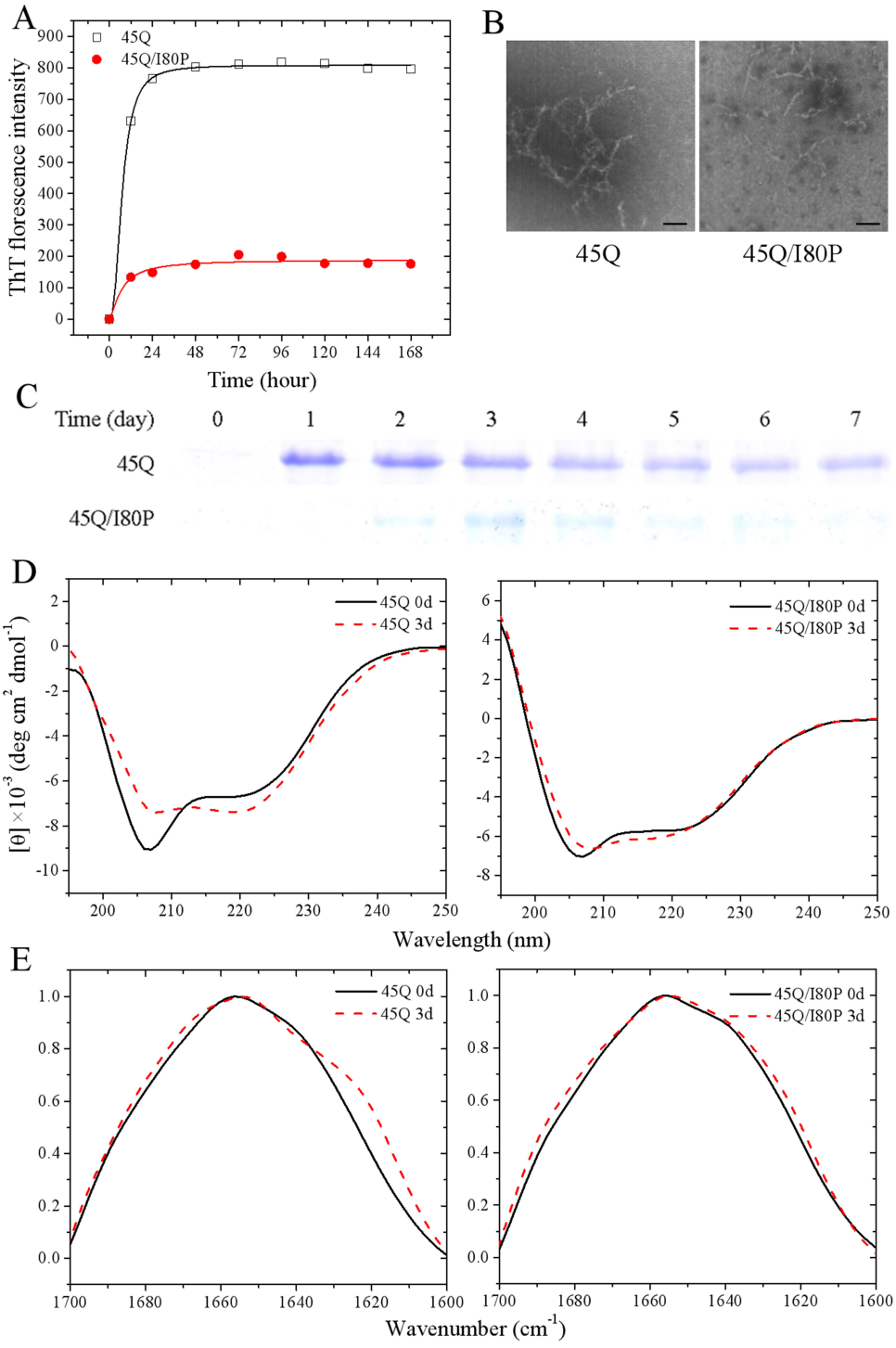

Figure 8. Proline mutation in fibril-forming motif inhibits the aggregation of expanded ataxin-3. (A) ThT binding assays of ataxin-3(45Q) and ataxin-3(45Q)/I80P. The kinetic curves are fitted with Hill function; (B) TEM measurements of ataxin-3(45Q) (left) and ataxin-3(45Q)/I80P (right); (C) Time-dependent SDS-PAGE analysis of sarkosyl-insoluble ataxin-3(45Q) and ataxin-3(45Q)/I80P. The scale bars represent 200 nm; (D) CD measurements of ataxin-3(45Q) (left) and ataxin-3(45Q)/I80P (right); (E) FTIR measurements of ataxin-3(45Q) (left) and ataxin-3(45Q)/I80P (right). TEM: Transmission electron microscopy; CD: circular dichroism; FTIR: Fourier transform infrared spectroscopy.

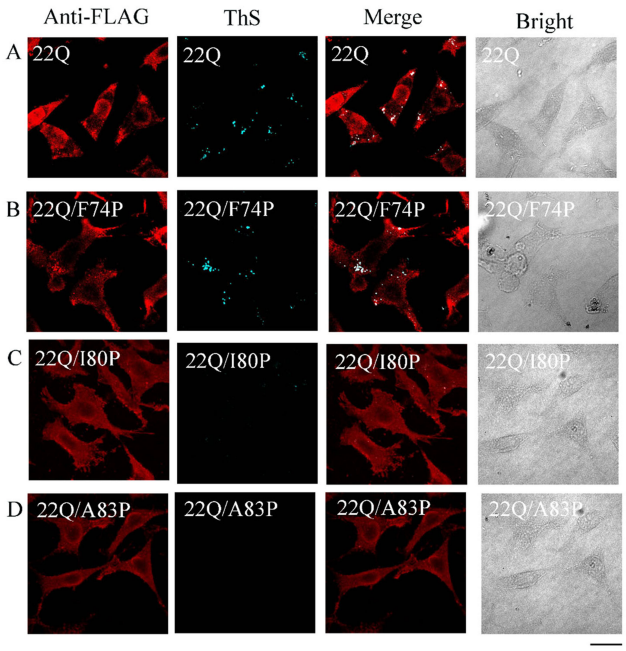

Figure 9. Sequence-dependent abnormal aggregation of human ataxin-3(22Q) takes place in SH-SY5Y cells. (A) Wild-type ataxin-3(22Q) and (B) ataxin-3(22Q)-F74P over-expressed in SH-SY5Y neuroblastoma cells formed aggregates in the cells. In contrast, no aggregates were observed in either (C) ataxin-3(22Q)-I80P or (D) ataxin-3(22Q)-A83P. SH-SY5Y cells were stained with 0.1% ThS, coimmunostained with primary monoclonal antibodies Anti-FLAG and secondary Alexa Fluo-546, and visualized by confocal microscopy. The scale bar represents 10 m. ThS: Thioflavin S.

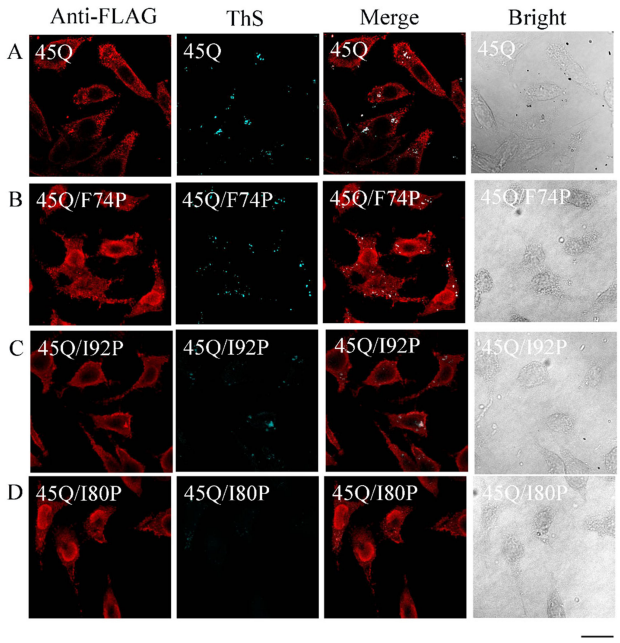

Figure 10. Sequence-dependent abnormal aggregation of human ataxin-3(45Q) takes place in SH-SY5Y cells. (A) Wild-type ataxin-3(45Q), (B) ataxin-3(45Q)-F74P mutant, (C) and ataxin-3(45Q)-I92P mutant overexpressed in SH-SY5Y cells formed aggregates in the cells; In contrast, no aggregates were observed in (D) ataxin-3(45Q)-I80P. The experimental conditions are the same as those in Figure 9.

and elucidated the fibril-forming motif as ^{79}VISNAL^{84}. Our conclusion is supported by the following literature:

(1) Bioinformatics studies suggest that the sequence 73-96 has the highest aggregation propensity, and point mutation experiments suggest that I77K/Q78K and W87K inhibit the aggregation of the Josephin domain[22].

(2) Molecular dynamics simulation suggests that the interaction of the Josephin domain is mainly driven by Arg101, followed by slower structural global rearrangements, involving the exposure to the solvent of ^{84}LKVW^{87}, which plays a key role in the aggregation of the Josephin domain[24].

(3) Limited proteolysis experiments combined with mass spectrometry analyses indicate that the trypsin proteolysis efficiency at Lys85 of expanded ataxin-3 is higher than non-expanded ataxin-3, providing evidence that an expanded polyQ tract alters the conformational dynamics of the Josephin domain. In addition, seeding experiments prove that peptide 73-96 promotes the aggregation of non-expanded and expanded ataxin-3[23].

(4) Hydrogen deuterium exchange coupled with mass spectrometry demonstrates that expanded polyQ tract increases the molecular mobility of two juxtaposed helices, 75-91 and 113-133. Fragment analysis shows that 76-81 in the two helices has the highest aggregation propensity, and proteinase K digestion indicates that residues 76-89 are the core of the Josephin domain fibril[47].

Since peptide ^{79}VISNAL^{84} is the fibril-forming motif of non-expanded ataxin-3, why is this peptide retained during evolution? We suggest that the peptide ^{79}VISNAL^{84} could participate in the following functions. The first possible function is the interaction of the Josephin domain and ubiquitin. Ataxin-3 is a ubiquitin-specific cysteine protease in the ubiquitin-proteasome system, and the residues Gln9, Cys14, His119, and Asn134 form a catalytic pocket to catalyze ubiquitination and Cys14 is the active site[48,49]. Ataxin-3 can bind to polyubiquitin chains with at least four ubiquitin units, and the N-terminal Josephin domain has two independent ubiquitin-binding sites. Ubiquitin-binding site 1 is near the catalytic pocket including Gln16, Ser76, Ile77, Gln78, Thr122, and Leu133, while ubiquitin-binding site 2 resides on the opposite side including Tyr27, Phe28, Val86, and Trp87[48,49]. The fibril-forming motif ^{79}VISNAL^{84} is just located between the ubiquitin-binding site 1 (Ser76, Ile77, and Gln78) and the ubiquitin-binding site 2 (Val86 and Trp87). The second possible function is nuclear export signal (NES). Josephin domain has two nuclear export signals, NES77 (^{77}IQVISNALKVWGL^{89}) and NES141 (^{141}ELISDTYLALFLAQLQQ E^{158})[50]. The fibril-forming motif ^{79}VISNAL^{84} is just located inside the NES77. The mutation of this fibril-forming motif could influence the cellular localization of ataxin-3, which could interact with mutant SOD1 and promote SOD1 aggregation[51].

A key limitation of this study is that we used *in vitro* reconstitution approaches to demonstrate that the proline mutation in the fibril-forming motif of the Josephin domain inhibits the aggregation of expanded ataxin-3, which shows some therapeutic promise. Direct *in vivo* biology investigations to connect this *in vitro* biophysical study with functions of fibril-forming motif of non-expanded ataxin-3 in living neurons are needed in the future.

In summary, we identified the fibril-forming motif of the Josephin domain as ^{79}VISNAL^{84}. By several structural and bioinformatic analyses, we discovered that proline mutation of the fibril-forming motif inhibited the misfolding of the expanded ataxin-3 in cells. This result is quite significant in the context of the present knowledge in the field that aggregation of ataxin-3 is the hallmark of the neurodegenerative

disease SCA3. Since this shows a proline mutation can inhibit such fibril formation, the study shows some therapeutic promise.

DECLARATIONS

Authors' contributions

Supervised the project: Hu HY, Liang Y
Designed the experiments: Meng SR, Hu HY, Liang Y
Performed the experiments:Meng SR, Ma C, Chen J, Wang LQ
Collected and analyzed the data, wrote the manuscript: Meng SR, Liang Y
All authors proofread and approved the manuscript.

Availability of data and materials

Not applicable.

Financial support and sponsorship

Liang Y acknowledges fundings from the National Natural Science Foundation of China (Nos. 32271326, 32071212, and 31770833); Wang LQ acknowledges financial support from the National Natural Science Foundation of China (No. 32201040), China Postdoctoral Science Foundation (Nos. 2021TQ0252 and 2021M700103), and the Fundamental Research Funds for the Central Universities (2042022kf1047); Hu HY acknowledges fundings from the National Natural Science Foundation of China (Nos. 31700669 and 31870764).

Conflicts of interest

The data that support the findings of this study are available from authors.

Ethical approval and consent to participate

Not applicable.

Consent for publication

Not applicable.

REFERENCES

1. Figueiredo F, Lopes-Marques M, Almeida B, et al. A robust assay to monitor ataxin-3 amyloid fibril assembly. *Cells* 2022;11:1969. DOI PubMed PMC
2. Toulis V, Casaroli-Marano R, Camós-Carreras A, et al. Altered retinal structure and function in Spinocerebellar ataxia type 3. *Neurobiol Dis* 2022;170:105774. DOI PubMed
3. do Carmo CostaM, Paulson HL. Toward understanding Machado-Joseph disease. *Prog Neurobiol* 2012;97:239-57. DOI PubMed PMC
4. Orr HT. Polyglutamine neurodegeneration: expanded glutamines enhance native functions. *Curr Opin Genet Dev* 2012;22:251-5. DOI PubMed PMC
5. Takiyama Y, Nishizawa M, Tanaka H, et al. The gene for Machado-Joseph disease maps to human chromosome 14q. *Nat Genet* 1993;4:300-4. DOI PubMed
6. Matos CA, de Macedo-Ribeiro S, Carvalho AL. Polyglutamine diseases: the special case of ataxin-3 and Machado-Joseph disease. *Prog Neurobiol* 2011;95:26-48. DOI PubMed
7. Margolis RL, Ross CA. Expansion explosion: new clues to the pathogenesis of repeat expansion neurodegenerative diseases. *Trends Mol Med* 2001;7:479-82. DOI PubMed
8. Haas E, Incebacak RD, Hentrich T, et al. A novel SCA3 knock-in mouse model mimics the human SCA3 Disease phenotype including neuropathological, behavioral, and transcriptional abnormalities especially in oligodendrocytes. *Mol Neurobiol* 2022;59:495-522. DOI PubMed PMC

9. Paulson H, Shakkottai V. Spinocerebellar ataxia type 3. GeneReviews. 2020. Available from: https://www.ncbi.nlm.nih.gov/books/NBK1196/. [Last accessed on 6 Jun 2024].
10. Lima M, Costa MC, Montiel R, et al. Population genetics of wild-type CAG repeats in the Machado-Joseph disease gene in Portugal. *Hum Hered* 2005;60:156-63. DOI PubMed
11. Ganev Y, Buhr TJ, Mahmood H. Manipulations of protective post-translational modifications of ataxin-3 as a possible treatment of SCA3. 2018. Available from: https://api.semanticscholar.org/CorpusID:195185159. [Last accessed on 6 Jun 2024].
12. Ricchelli F, Fusi P, Tortora P, et al. Destabilization of non-pathological variants of ataxin-3 by metal ions results in aggregation/fibrillogenesis. *Int J Biochem Cell Biol* 2007;39:966-77. DOI PubMed
13. Marchal S, Shehi E, Harricane MC, et al. Structural instability and fibrillar aggregation of non-expanded human ataxin-3 revealed under high pressure and temperature. *J Biol Chem* 2003;278:31554-63. DOI PubMed
14. Gales L, Cortes L, Almeida C, et al. Towards a structural understanding of the fibrillization pathway in Machado-Joseph's disease: trapping early oligomers of non-expanded ataxin-3. *J Mol Biol* 2005;353:642-54. DOI PubMed
15. Ellisdon AM, Thomas B, Bottomley SP. The two-stage pathway of ataxin-3 fibrillogenesis involves a polyglutamine-independent step. *J Biol Chem* 2006;281:16888-96. DOI PubMed
16. Masino L, Nicastro G, De Simone A, Calder L, Molloy J, Pastore A. The Josephin domain determines the morphological and mechanical properties of ataxin-3 fibrils. *Biophys J* 2011;100:2033-42. DOI PubMed PMC
17. Conchillo-Solé O, de Groot NS, Avilés FX, Vendrell J, Daura X, Ventura S. AGGRESCAN: a server for the prediction and evaluation of "hot spots" of aggregation in polypeptides. *BMC Bioinformatics* 2007;8:65. DOI PubMed PMC
18. Fernandez-Escamilla AM, Rousseau F, Schymkowitz J, Serrano L. Prediction of sequence-dependent and mutational effects on the aggregation of peptides and proteins. *Nat Biotechnol* 2004;22:1302-6. DOI PubMed
19. Maurer-Stroh S, Debulpaep M, Kuemmerer N, et al. Exploring the sequence determinants of amyloid structure using position-specific scoring matrices. *Nat Methods* 2010;7:237-42. DOI PubMed
20. Trovato A, Seno F, Tosatto SC. The PASTA server for protein aggregation prediction. *Protein Eng Des Sel* 2007;20:521-3. DOI PubMed
21. Tartaglia GG, Vendruscolo M. The Zyggregator method for predicting protein aggregation propensities. *Chem Soc Rev* 2008;37:1395-401. DOI PubMed
22. Masino L, Nicastro G, Calder L, Vendruscolo M, Pastore A. Functional interactions as a survival strategy against abnormal aggregation. *FASEB J* 2011;25:45-54. DOI PubMed PMC
23. Scarff CA, Almeida B, Fraga J, Macedo-Ribeiro S, Radford SE, Ashcroft AE. Examination of ataxin-3 (atx-3) aggregation by structural mass spectrometry techniques: a rationale for expedited aggregation upon polyglutamine (polyQ) expansion. *Mol Cell Proteomics* 2015;14:1241-53. DOI PubMed PMC
24. Deriu MA, Grasso G, Licandro G, et al. Investigation of the Josephin Domain protein-protein interaction by molecular dynamics. *PLoS One* 2014;9:e108677. DOI PubMed PMC
25. Sawaya MR, Sambashivan S, Nelson R, et al. Atomic structures of amyloid cross-beta spines reveal varied steric zippers. *Nature* 2007;447:453-7. DOI PubMed
26. Meng SR, Zhu YZ, Guo T, Liu XL, Chen J, Liang Y. Fibril-forming motifs are essential and sufficient for the fibrillization of human Tau. *PLoS One* 2012;7:e38903. DOI PubMed PMC
27. Thompson MJ, Sievers SA, Karanicolas J, Ivanova MI, Baker D, Eisenberg D. The 3D profile method for identifying fibril-forming segments of proteins. *Proc Natl Acad Sci U S A* 2006;103:4074-8. DOI PubMed PMC
28. Goldschmidt L, Teng PK, Riek R, Eisenberg D. Identifying the amylome, proteins capable of forming amyloid-like fibrils. *Proc Natl Acad Sci U S A* 2010;107:3487-92. DOI PubMed PMC
29. Ivanova MI, Sievers SA, Guenther EL, et al. Aggregation-triggering segments of SOD1 fibril formation support a common pathway for familial and sporadic ALS. *Proc Natl Acad Sci U S A* 2014;111:197-201. DOI PubMed PMC
30. Nelson R, Sawaya MR, Balbirnie M, et al. Structure of the cross-beta spine of amyloid-like fibrils. *Nature* 2005;435:773-8. DOI PubMed PMC
31. Kuhlman B, Baker D. Native protein sequences are close to optimal for their structures. *Proc Natl Acad Sci U S A* 2000;97:10383-8. DOI PubMed PMC
32. Toyama BH, Weissman JS. Amyloid structure: conformational diversity and consequences. *Annu Rev Biochem* 2011;80:557-85. DOI PubMed PMC
33. Kannan R, Raju M, Sharma KK. The critical role of the central hydrophobic core (residues 71-77) of amyloid-forming αA66-80 peptide in α-crystallin aggregation: a systematic proline replacement study. *Amyloid* 2014;21:103-9. DOI PubMed PMC
34. Chang HY, Lin JY, Lee HC, Wang HL, King CY. Strain-specific sequences required for yeast [PSI+] prion propagation. *Proc Natl Acad Sci U S A* 2008;105:13345-50. DOI PubMed PMC
35. Williams AD, Portelius E, Kheterpal I, et al. Mapping abeta amyloid fibril secondary structure using scanning proline mutagenesis. *J Mol Biol* 2004;335:833-42. DOI PubMed
36. Tao H, Liu W, Simmons BN, Harris HK, Cox TC, Massiah MA. Purifying natively folded proteins from inclusion bodies using sarkosyl, Triton X-100, and CHAPS. *Biotechniques* 2010;48:61-4. DOI PubMed
37. Fitzpatrick AWP, Falcon B, He S, et al. Cryo-EM structures of tau filaments from Alzheimer's disease. *Nature* 2017;547:185-90. DOI
38. Yang Y, Shi Y, Schweighauser M, et al. Structures of α-synuclein filaments from human brains with Lewy pathology. *Nature*

2022;610:791-5. DOI PubMed PMC

39. Hu JY, Zhang DL, Liu XL, et al. Pathological concentration of zinc dramatically accelerates abnormal aggregation of full-length human Tau and thereby significantly increases Tau toxicity in neuronal cells. *Biochim Biophys Acta Mol Basis Dis* 2017;1863:414-27. DOI PubMed
40. Xu WC, Liang JZ, Li C, et al. Pathological hydrogen peroxide triggers the fibrillization of wild-type SOD1 via sulfenic acid modification of Cys-111. *Cell Death Dis* 2018;9:67. DOI PubMed PMC
41. Wang K, Liu JQ, Zhong T, et al. Phase separation and cytotoxicity of tau are modulated by protein disulfide isomerase and s-nitrosylation of this molecular chaperone. *J Mol Biol* 2020;432:2141-63. DOI PubMed
42. Dai B, Zhong T, Chen ZX, et al. Myricetin slows liquid-liquid phase separation of Tau and activates ATG5-dependent autophagy to suppress Tau toxicity. *J Biol Chem* 2021;297:101222. DOI PubMed PMC
43. Teng PK, Eisenberg D. Short protein segments can drive a non-fibrillizing protein into the amyloid state. *Protein Eng Des Sel* 2009;22:531-6. DOI PubMed PMC
44. Robertson AL, Headey SJ, Saunders HM, et al. Small heat-shock proteins interact with a flanking domain to suppress polyglutamine aggregation. *Proc Natl Acad Sci U S A* 2010;107:10424-9. DOI PubMed PMC
45. Masino L, Nicastro G, Menon RP, Dal Piaz F, Calder L, Pastore A. Characterization of the structure and the amyloidogenic properties of the Josephin domain of the polyglutamine-containing protein ataxin-3. *J Mol Biol* 2004;344:1021-35. DOI PubMed
46. Sicorello A, Różycki B, Konarev PV, Svergun DI, Pastore A. Capturing the conformational ensemble of the mixed folded polyglutamine protein ataxin-3. *Structure* 2021;29:70-81.e5. DOI PubMed
47. Lupton CJ, Steer DL, Wintrode PL, Bottomley SP, Hughes VA, Ellisdon AM. Enhanced molecular mobility of ordinarily structured regions drives polyglutamine disease. *J Biol Chem* 2015;290:24190-200. DOI PubMed PMC
48. Nicastro G, Masino L, Esposito V, et al. Josephin domain of ataxin-3 contains two distinct ubiquitin-binding sites. *Biopolymers* 2009;91:1203-14. DOI PubMed
49. Nicastro G, Menon RP, Masino L, Knowles PP, McDonald NQ, Pastore A. The solution structure of the Josephin domain of ataxin-3: structural determinants for molecular recognition. *Proc Natl Acad Sci U S A* 2005;102:10493-8. DOI PubMed PMC
50. Antony PMA, Mäntele S, Mollenkopf P, et al. Identification and functional dissection of localization signals within ataxin-3. *Neurobiol Dis* 2009;36:280-92. DOI PubMed
51. Wang H, Ying Z, Wang G. Ataxin-3 regulates aggresome formation of copper-zinc superoxide dismutase (SOD1) by editing K63-linked polyubiquitin chains. *J Biol Chem* 2012;287:28576-85. DOI PubMed PMC